ISSN 0915-633X

NATIONAL INSTITUTE FOR FUSION SCIENCE

Simulated Impurity Transport in LHD from MIST

J.E. Rice

(Received - Apr. 13, 1998)

NIFS-548 May 1998

This report was prepared as a preprint of work performed as a collaboration reserch of the National Institute for Fusion Science (NIFS) of Japan. This document is intended for infomation only and for future publication in a journal after some rearrangements of its contents.

Inquiries about copyright and reproduction should be addressed to the Research Information Center, National Institute for Fusion Science, Oroshi-cho, Toki-shi, Gifu-ken 509-02 Japan.

RESEARCH REPORT
NIFS Series

NAGOYA, JAPAN

Simulated Impurity Transport in LHD from MIST

J. E. Rice*

NIFS

Abstract

The impurity transport code MIST and atomic physics package LINES are used to calculate the time evolution of charge state density profiles, individual line emissivity profiles and total radiated power profiles for impurities in LHD plasmas. Three model LHD plasmas are considered; a high density, low temperature case, a low density, high temperature case and the initial LHD start-up plasma (500 kW ECH), using impurity transport coefficient profiles from Heliotron E. The elements oxygen, neon, scandium, iron, nickel and molybdenum are considered, both injected and in steady state.

keywords: LHD, impurity transport, impurity radiation

* permanent address: MIT PSFC, Cambridge, MA, USA

Introduction

Impurities in LHD are a concern from the potential radiation losses, especially during plasmas with long particle confinement. Impurity levels in the plasma are a result of two factors: impurity sources from plasma contact with the divertor regions and walls, and the subsequent transport into the plasma core. The sources are a function of edge plasma conditions and the plasma facing components' composition and geometry, while the transport inside the plasma is governed by transport coefficients (usually characterized by a diffusion coefficient and a convection velocity) often dominated by anomalous (non-neoclassical) effects. The transport coefficients may be isolated by impurity injection experiments, where trace amounts of non-intrinsic, non-recycling impurities are introduced by laser blow-off. The most thorough determination of the transport coefficient profiles requires measurement of the time evolution of impurity emission across the whole plasma cross section, which involves the use of spatially resolving x-ray, VUV and visible diagnostics. Choice of the appropriate element(s) for injection is largely determined by the electron temperature profile, in conjunction with the wavelength coverage of the available spectrometer systems. The appropriate impurity density in the plasma for the measurement must be kept low enough not to perturb the plasma through radiation losses, yet high enough for the spectrometer system sensitivities. To produce this ideal impurity density in the plasma, the amount to be injected must be determined from geometric considerations and edge plasma screening, which may be anywhere from 1-100 %.

In this report three model LHD plasmas are considered; a high density, low temperature case, a low density, high temperature case and the initial LHD startup plasma with low temperature and density. Impurity transport coefficient profiles from Heliotron E are used as a starting point. Charge state density profiles, individual line emissivity profiles, line integrated brightnesses and total power radiation from the elements oxygen, neon, scandium, iron, nickel and molybdenum are considered.

Code Description

The 1D impurity transport code MIST[1] has been used to determine the time evolution of charge state density profiles for user specified machine size, electron density and temperature profiles (neutral hydrogen density profiles if charge-exchange is important for ionization balance) and transport coefficient profiles for any given element. MIST solves the equation

$$\frac{\partial n_Z}{\partial t} = \frac{-1}{r}\frac{\partial}{\partial r}(r\Gamma_Z) + \alpha_{Z+1}n_{Z+1} - (\alpha_Z + S_Z)n_Z + S_{Z-1}n_{Z-1} + source$$

where S is the total ionization rate (direct collisional ionization and excitation-autoionization), α is the total recombination rate (radiative, dielectronic and charge-exchange) and

$$\Gamma = -D(r)\frac{\partial n_Z}{\partial r} + v(r)n_Z \qquad (2)$$

where D(r) is the diffusion coefficient and v(r) is the convection velocity. The steady state solution may be determined, or the time dependent solution from a delta function source, to model impurity injection. The recycling coefficient may be set to 100 % to simulate gaseous injection.

In the original version of MIST, S and α were taken from ADPAK[2]. However, in higher Z elements, these dielectronic recombination rates may not be accurate, and excitation-autoionization, which is ignored in ADPAK, can dominate the ionization process for certain charge states[3,4]. The latest rates for selected elements can be found in Refs.[4,5]. The transport coefficient profiles, D(r) and v(r), have been determined from laser blow-off experiments in many tokamaks (see Refs.[6,7] and references therein) and in Heliotron-E[8,9], and are generally regarded as anomalous, far from the neo-classical values[10]. Many different forms for D and v have been

considered, and some general results for the relation between impurity density profile shape and the impurity confinement time, τ_I, and D and v are summarized here[11]. For the case with D(r) = constant and v = 0, the total impurity density profile, n_I = constant, and τ_I = .17 a^2/D, where a is the minor radius. For the case with D(r) = constant and v(r) = v_0 r/a, n_I = exp-[S(r/a)^2] and

$$\tau_I = \frac{(77+S^2)}{(56+S^2)} \frac{(e^S - S - 1)}{(4S^2)} \frac{a^2}{D} \tag{3}$$

where the peaking factor S = a v_0/(2D). While this linearly increasing convection velocity profile provides ease in analytic computation of τ_I and n_I, it is an unrealistic shape and has never been measured experimentally. For the case of v = -S D d(ln n_e)/dr, n_I(r) = $[n_e(r)]^S$.

Once the charge state density profiles are determined from MIST, individual line emissivity profiles are calculated from the IDL procedure LINES[12]. LINES calculates individual line (E1, E2, M1 M2) emissivity profiles from n_e, T_e, n_H and n_Z profiles, for upper levels populated by collisional excitation, radiative, dielectronic and charge-exchange recombination and inner shell ionization. Collisional excitation rates for H-, Li-, Ne- and Na-like ions (and estimates for other ions) are taken from Ref.[13], collisional excitation, radiative and dielectronic recombination and inner shell ionization rates for He-like ions have been used from Ref.[14], dielectronic and inner-shell satellites have been treated in a manner similar to that found in Ref.[15] with rates from Ref.[16] and population by charge-exchange recombination has been included following Refs.[17,18]. Excitation rates for lines from eight molybdenum charge states, including the effects of configuration interaction, were taken from Ref.[3]. From the calculated emissivity profiles the chordal brightnesses may be determined by integration along the line of sight. Comparison with observed brightnesses can determine absolute charge state density profiles, and the transport coefficient profiles. Total radiated power from a given element may then be determined in a rigorous fashion by adding up all the power radiated by all important lines in all charge states across the plasma volume. An easier approach is to

employ the average ion model[2] (including newer rates from Ref.[5]), which ignores transport and assumes coronal equilibrium.

Calculation of Impurity Density/Emissivity Profiles

Three model LHD plasmas will be considered; a high density, low temperature discharge, a low density, high temperature discharge and a model start-up plasma. The first two cases are produced by 5 MW of ECH and 20 MW of NBI (25 MW total), and the LHD start-up plasma has 500 kW of ECH input. Temperature and density profiles[19,20] are shown in Fig.1, where an average minor radius of 60 cm has been used. The high density case has $n_e \sim 1 \times 10^{14}$ cm^{-3} over most of the profile, with a central electron temperature of 4 keV. The low density case has $n_e \sim 3 \times 10^{13}$ cm^{-3} over most of the profile, with a central electron temperature of 7.5 keV. The start-up plasma has a similar low density, with a central electron temperature of slightly over 1 keV. Lacking any *a priori* calculations of the expected impurity transport coefficient profiles for LHD, representative values have been taken from Heliotron-E results[8,9], and are shown in Fig.2. For the high density case in Heliotron-E, the transport was modelled by spatially uniform diffusion with a coefficient of 1250 cm^2/s, and an inward convection velocity of 300 (r/a) cm/s. This severe inward convection velocity near the plasma center produces a large peaking factor of 7.5 for LHD, and yields (from Eq.(3)) an impurity confinement time of 28 s: this extreme value is partly due to the large size of LHD. Since this shape of convection velocity profile has never been verified experimentally, a more moderate profile will also be considered, with substantial convection only near the plasma edge, following tokamak observations[6,7]. These modified transport coefficient profiles give rise to an impurity confinement time of $\sim$ 2 s. For the low density plasmas of Heliotron-E, the transport was modelled by higher diffusion with no evidence for convection, also shown in Fig.2. This case has a confinement time of 400 ms for LHD.

Given the electron temperature and density profiles, and the impurity transport coefficient profiles, charge state density and individual line emissivity profiles may be calculated. As a starting point, differences in impurity transport will be demonstrated for the two different high electron density case impurity transport coefficient profiles of Fig.2 for the element scandium. Scandium has been chosen since it is a non-intrinsic non-recycling impurity which is easy to inject via laser blow-off. Results for the steady state charge state density profiles for hydrogen-, helium- and lithiumlike scandium are shown in Fig.3. For the modified transport coefficient profiles, the edge scandium densities are 2 orders of magnitude larger, and the strong inward convection of the unmodified case makes lithiumlike scandium a central rather than edge state. These different density profiles are reflected in the concomitant emissivity profiles of the three brightest lines from these charge states, shown in Fig.4. The emission of the Li-like line at 279 Å is 2 orders of magnitude more intense near the plasma edge in the modified case. For simulation of impurity injection experiments, MIST may be run in the time dependent mode, with no recycling. The time evolution of the total scandium density (summed over all charge states) profiles is shown in Fig.5, at seven different times after the injection time, for the high electron density, modified and unmodified transport cases. In the top frame (unmodified), the scandium density profile never reaches a steady state, and is continually peaking up. In the modified case (bottom frame), the profile reaches its steady state, generally flat shape in under 500 ms. The times between the profiles in the two cases are the same. Note that the central scandium density is a factor of 50 lower at 500 ms in the modified case. The top frame demonstrates how strong a peaking factor of 7.5 is. The emissivity profiles of the three main lines from these charge states exhibit similar characteristics. Shown in Fig.6 are the normalized central chord brightness time histories (emissivity profiles integrated along a central line of sight) of the same three emission lines from Fig.4. In the top (bottom) frame is the unmodified (modified) case; it's evident that the time history of the lithiumlike line is the most sensitive to these differences in transport.

For the low density, high electron temperature case, with diffusion only (Figs.1

and 2), the corresponding steady state scandium density profiles (including the fully stripped state) are shown in Fig.7. In this case, even the hydrogenlike level is burned through, and perhaps scandium is not the best element for determining the transport coefficients at the plasma center. At this temperature, molybdenum (or niobium) has the lithiumlike state at the plasma center, whose most intense line is at 58.5 Å, in the VUV. As seen in Fig.8, there are many charge states of molybdenum across the plasma profile. There are several convenient emission lines[3] from these charge states in the high temperature case, as shown in Fig.9, also distributed across the profile. The time histories of the central chord brightnesses of these lines for a molybdenum injection into the high temperature case plasma are shown in Fig.10. The same plot with normalized brightnesses is shown in Fig.11, where the sequential peaking of the charge states is apparent. The decay time (confinement time) of all the lines after t = 300 ms is about 400 ms. If x-ray spectrometers are available for the central state measurements, then a less radiative, lower z element such as nickel might be a better choice for the high temperature plasma case. Shown in Fig.12 are the steady state charge state density profiles for nickel near the plasma center, and the hydrogen like state, whose strongest emission line is at 1.53 Å, is not burned through.

Total Radiated Power

A convenient, although approximate method for computing the radiated power emissivity profiles is by using the power loss coefficient (cooling curves) from the average ion model model of ADPAK[2]. Cooling curves as a function of electron temperature for molybdenum, iron and oxygen from ADPAK, along with a more recent and comprehensive calculation for molybdenum[22] are shown in Fig.13. The minima in all these curves correspond to closed electronic shells. The thin solid line for molybdenum (from ADPAK) is shifted to the right because the total ionization rate was underestimated by ignoring excitation autoionization[4]: in a strange instance of *déjà vu*, this same case was treated in the appendix of Ref.[2]. These

differences can give rise to varying conclusions about total radiated power from molybdenum. By multiplying these curves by the electron and impurity densities, the radiated power emissivity as a function of electron temperature may be determined. If the electron temperature profile is known, the radiated power emissivity profile may be calculated under the assumption of coronal equilibrium. For the two 25 MW input power plasmas of Fig.1, the molybdenum radiation profiles are shown in Fig.14, where the total molybdenum density profile was taken to be 10^{-4} times the electron density profile in the two cases. Both profiles peak near where the electron temperature is 400 eV. The total power radiated may be determined by integrating over the plasma cross section, where it is assumed that LHD is a torus with an average minor radius of 60 cm and a major radius of 390 cm. The total radiated power for the high electron density case is 2.1 MW, nearly 10% of the total input power, but only 150 kW, a negligible amount, in the low electron density case. Similar plots for the intrinsic impurities oxygen and iron are shown in Figs.15 and 16 for the high electron density case, with the total impurity density equal to 10^{-3} times the electron density profile. For oxygen, the radiated power is mere 75 kW, while for iron the total radiated power is 7.5 MW, about a third of the input power.

For the LHD start-up plasma of Fig.2, the radiated power density profiles for oxygen are shown in Fig.17, for a central oxygen density of 10^{-3} times the central electron density. Two cases are shown; the solid curve is for a flat total oxygen density profile, which would result from diffusion-only transport, and the dash-dot-dot-dot curve is for a total oxygen density profile with the same shape as the electron density profile, which would result from a little edge convection. In the flat profile case, 20% of the 500 kW input power is radiated by a concentration of .1% oxygen. For .01% iron in the same plasma, 150 kW are radiated, as shown in Fig.18. A more rigorous, but more time consuming approach to the radiated power density profile calculation is to run MIST and LINES for all emission lines of all charge states, multiply by the energy per photon and then sum over all the lines. This is the proper approach when the transport times are of order recombination times,

especially near the plasma edge, where the charge state distribution is out of coronal equilibrium, and the strongly radiating states are moved to lower temperature regions. For the start-up profiles of Fig.1, with the low density transport coefficients of Fig.2, the edge oxygen charge state density profiles are shown in Fig.19. The corresponding emissivity profiles of all the major lines of each of the charge states between hydrogenlike and boronlike are shown in Fig.20. The total emissivity is dominated by the lithiumlike doublet (near 1034 Å) and the berylliumlike line at 629.7 Å (shown separately by the thin line). The radiated power density profiles for these charge states are shown in Fig.21, again dominated by the same few lines. Shown for comparison is the ADPAK calculation from Fig.17, which is in fair agreement with the total of all charge state power emissivities. Differences between the two curves in radius may be attributed to the effects of transport, while differences in amplitude may be due to the modelling of the populations of the line upper levels. Bear in mind that in the LINES calculation, a total of only 26 individual lines from 7 charge states were included. The same three plots for neon are shown in Figs.22-24.

Gas puffing experiments may be simulated using MIST in time dependent mode, but with 100 % recycling. For the start-up plasma profiles of Fig.1 and the low density transport coefficients of Fig.2, the time evolution of the total neon density profiles for an injection of 10^{18} neon atoms is shown in Fig.25. Even with this relatively fast impurity transport, the steady state density profile is not reached until 500 ms for this recycling gas, in contrast to the case of Fig.11, where for the same transport coefficients, the steady state profile *shape* was reached in 300 ms. The time histories of the central chord brightnesses of representative lines from several neon charge states are shown in Fig.26. The three edge states quickly peak about 10 ms after the neon puff, while the more central states take a few hundred ms to reach their maxima. The power emissivity profiles at 10 and 100 ms after the puff are shown in Figs.27 and 28, respectively. At 10 ms, the radiation is sharply peaked at the edge, and then spreads toward the center as time progresses. The time evolution of the total radiated power is plotted in Fig.29, where the sum of

individual lines from LINES is compared to the ADPAK results. In both cases there is a very large spike in the radiation around 10 ms, where the total input power of 500 kW may be lost. Differences between the two curves before 50 ms are due to the effects of transport, while differences in the total magnitude late in time are due to both the effects of transport and differences in line upper level population modelling. In real gas puff experiments, the source is actually spread out in time, because of conduction in the gas lines, the finite opening time of the gas valve and the relatively low temperature of the gas, so a large spike in the radiation is not likely to occur. Spreading out the gas puff over 30 ms reduces the magnitude of the spike, as seen in Fig.30.

Conclusions

The codes MIST and LINES have been used to simulate impurity transport in LHD. Several different electron density and temperature profiles have been considered, with impurity transport coefficients taken from Heliotron-E. If the edge penetration is high enough, impurity transport coefficients in LHD may be determined from injection of scandium, nickel and/or molybdenum/niobium. Intrinsic iron may be a problem during high density operation and should be kept below 10^{-3} times the electron density. Intrinsic oxygen may be a problem during the start-up phase and should be kept below $5\text{x}10^{-3}$ n_e.

Acknowledgements

The use of MIST from PPPL is gratefully acknowledged. The author would like to thank Profs. Motojima and Noda of NIFS for the invitation to work at LHD, Prof. Okamura for assistance with the computer systems and Drs. Terry and Goetz of MIT for help with MIST.

References

[1] R.A.Hulse, Nucl. Tech./Fus. **3**, 259 (1983)

[2] D.E.Post et al., At. Data Nucl. Data Tables **20**, 397 (1977)

[3] J.E.Rice et al., J. Phys. B. **29**, 2191 (1996)

[4] K.B.Fournier et al., Phys. Rev. A **54**, 3870 (1996)

[5] K.B.Fournier et al., submitted to At. Data Nucl. Data Tables (1998)

[6] D.Pasini et al., Plasma Phys. Controlled Fusion **34**, 677 (1992)

[7] J.E.Rice et al., Phys. Plasmas **4**, 1609 (1997)

[8] J.E.Rice et al., Nucl. Fusion **24**, 1205 (1984)

[9] H. Kaneko et al., Nucl. Fusion **27**, 1075 (1987)

[10] R.Hawryluk et al., Nucl. Fusion **19**, 607 (1979)

[11] F.Seguin et al., Phys. Rev. Lett. **51**, 455 (1983)

[12] M.A.Graf, Ph.D. Dissertation, MIT (1995)

[13] R. Mewe, Astron. Astrophys. **20**, 99 (1972)

[14] R. Mewe and J.Schrijver, Astron. Astrophys. **65**, 99 (1978)

[15] F.Bombarda et al., Phys. Rev. A **37**, 504 (1988)

[16] L.A.Vainshtein and U.I.Safronova, At. Data Nucl. Data Tables **21**, 49 (1978)

[17] T.Kato et al., Phys. Rev. A **44**, 6776 (1991)

[18] J.E.Rice, E.S.Marmar, E.Källne and J.Källne, Phys. Rev. A **35**, 3033 (1987)

[19] K. Yamazaki and T. Amano, Nucl. Fusion **32**, 633 (1992)

[20] H. Yamada and J. Miyazawa, from the plasma profile calculator found at http://lhdmemo.nifs.ac.jp

[21] J.E.Rice et al., J. Phys. B. **28**, 893 (1995)

[22] K.B.Fournier et al., Nucl. Fusion **37**, 825 (1997)

Figure Captions

Fig. 1 Modelled electron temperature and density profiles. Dashed lines are for the high density case, solid lines are for the low density case, and the dash-dot-dot-dot lines are for the LHD start-up case.

Fig. 2 Assumed impurity diffusion coefficient and convection velocity profiles. Dotted lines are for the high density case, dashed lines are for the modified high density case and solid lines are for the low density cases. Resultant impurity confinement times are shown in the bottom frame inset.

Fig. 3 Calculated scandium charge state density profiles for the high electron density cases. Solid, dashed and dotted lines are for hydrogen-, helium- and lithiumlike scandium, respectively. The thick lines are for the modified (dashed lines) transport coefficient profiles of Fig.2, thin lines for the unmodified (dotted) profiles.

Fig. 4 Calculated scandium emissivity profiles for the high electron density case. Solid, dashed and dotted lines are for the most intense lines from the hydrogen-, helium- and lithiumlike charge states at 2.74, 2.87[21] and 279 Å, respectively. The thick lines are for the modified (dashed lines) transport coefficient profiles of Fig.2, thin lines for the unmodified (dotted) profiles.

Fig. 5 Calculated time evolution of the total scandium density profiles in the high density case, at several times (noted in the bottom frame) after the 'injection'. The top (bottom) frame is from the unmodified (modified) transport coefficients of Fig.2. The time intervals in both cases are the same.

Fig. 6 Calculated central chord scandium brightness time histories in the high density case. Solid, dashed and dotted lines are for the most intense lines from the hydrogen-, helium- and lithiumlike charge states at 2.74, 2.87 and 279 Å, respectively. The top (bottom) frame is from the unmodified (modified) transport

coefficients of Fig.2.

Fig. 7 Calculated scandium charge state density profiles for the low electron density case. Dash-dot-dot-dot, solid, dashed and dotted lines are for fully stripped, hydrogen-, helium- and lithiumlike scandium, respectively.

Fig. 8 Calculated steady state molybdenum charge state density profiles for the low electron density, high electron temperature case. The isosequence labels are shown, e.g. lithiumlike molybdenum (dotted) is a central state, fluorinelike molybdenum (dashed) is located about half way out, and potassiumlike molybdenum (solid) is an edge state.

Fig. 9 Calculated steady state molybdenum emissivity profiles for the low electron density case. The lithiumlike (dotted) line at 58.5 Å emanates from the plasma center, the neonlike line (solid) at 4.63Å comes from halfway out, and the copperlike line (dotted) at 373 Å is from the extreme perifery of the plasma.

Fig. 10 Calculated central chord molybdenum brightness time histories in the low density case. The lines from copperlike (dotted, 373 Å), magnesiumlike (dashed, 128 Å), sodiumlike (dotted, 116 and 3.79 Å), neonlike (solid, 4.63 Å), fluorinelike (dashed, 3.61 Å) and lithiumlike molybdenum (dotted, 58.5 Å) peak sequentially in time.

Fig. 11 Normalized central chord molybdenum brightness time histories in the low density case, with the same legend as in Fig.10.

Fig. 12 Calculated nickel charge state density profiles for the low electron density case. Solid, dashed and dotted lines are for hydrogen-, helium- and lithiumlike nickel, respectively.

Fig. 13 Total power loss coefficient as a function of electron temperature for

molybdenum (solid), iron (dashed) and oxygen (dash-dot-dot-dot). The thin solid line is from ADPAK calculations which do not include excitation autoionization.

Fig. 14 Calculated molybdenum radiated power emissivity profiles from Ref.[22], assuming a total molybdenum density of 10^{-4} times the electron density, for the two 25 MW input power cases of Fig.1.

Fig. 15 Calculated oxygen radiated power emissivity profile from ADPAK, assuming a total oxygen density of 10^{-3} times the electron density, for the high density 25 MW input power case of Fig.1.

Fig. 16 Calculated iron radiated power emissivity profile from ADPAK, assuming a total iron density of 10^{-3} times the electron density, for the high density 25 MW input power case of Fig.1.

Fig. 17 Calculated oxygen radiated power emissivity profiles from ADPAK, assuming a total central oxygen density of 10^{-3} times the central electron density, for the .5 MW input power start-up case of Fig.1. The solid curve is for a flat total oxygen density profile and the dash-dot-dot-dot curve is for a total oxygen density profile with the same shape as the electrons.

Fig. 18 Calculated iron radiated power emissivity profile from ADPAK assuming a total iron density of 10^{-4} times the electron density, for the .5 MW input power start-up plasma of Fig.1.

Fig. 19 Calculated steady state oxygen charge state density profiles for the start-up plasma case, using the low density transport coefficients of Fig.2. The isosequence labels are shown, e.g. fully stripped oxygen (solid) is a central state, hydrogen- and heliumlike (dashed and dotted) cover nearly half of the plasma and the lower states are all bunched in the outer 10 cm.

Fig. 20 Calculated steady state oxygen emissivity profiles for the same case as in Fig.19. All emission lines of each charge state are summed up and shown as one curve with the charge state label. The lithiumlike (dash-dot-dot-dot), berylliumlike (solid) and boronlike (dashed) lines dominate the total emissivity. The individual OV line at 629.7 Å (thin solid line) accounts for most of the berylliumlike radiation.

Fig. 21 Calculated oxygen total radiated power profiles for the same case as in Fig.20, for the individual charge states, and the coronal ADPAK curve (thin dash-dot-dot-dot) for comparison.

Fig. 22 Calculated steady state neon charge state density profiles for the start-up plasma case, using the low density transport coefficients of Fig.2. The isosequence labels are shown, e.g. fully stripped neon (solid) is a central state, hydrogen- and heliumlike (dashed and dotted) cover nearly half of the plasma and the lower states are all bunched in the outer 10 cm.

Fig. 23 Calculated steady state neon emissivity profiles for the same case as in Fig.22. The lithiumlike (dash-dot-dot-dot), berylliumlike (solid) and boronlike (dashed) lines dominate the total emissivity. The individual NeVII line at 465.2 Å (thin solid line) accounts for most of the berylliumlike radiation.

Fig. 24 Calculated neon total radiated power profiles for the same case as in Fig.23, for the individual charge states, and the coronal ADPAK curve (thin dash-dot-dot-dot) for comparison.

Fig. 25 Calculated time evolution of the total neon density profiles in the start-up case, at several times after the 'gas puff'.

Fig. 26 Calculated central chord neon brightness time histories in the start-up case. The lines from B-like (solid, 402 Å), Be-like (solid, 465 Å), Li-like (dash-dot-dot-dot 770 Å), He-like (dotted, 13.4 Å) and Hy-like neon (dot-dash 12.1 Å) peak

sequentially in time.

Fig. 27 Calculated neon total radiated power profiles for the same case as in Fig.26, at 10 ms, for the individual charge states, and the coronal ADPAK curve (thin dash-dot-dot-dot) for comparison.

Fig. 28 Calculated neon total radiated power profiles for the same case as in Fig.26, at 100 ms, for the individual charge states, and the coronal ADPAK curve (thin dash-dot-dot-dot) for comparison.

Fig. 29 The time evolution of the total radiated power from all neons lines. The solid curve is for the total of lines in Figs.27 and 28, and the dash-dot-dot-dot curve is from ADPAK.

Fig. 30 The time evolution of all lines from Fig.29 (solid) and the same with an average puff over 30 ms (dash-dot-dot-dot).

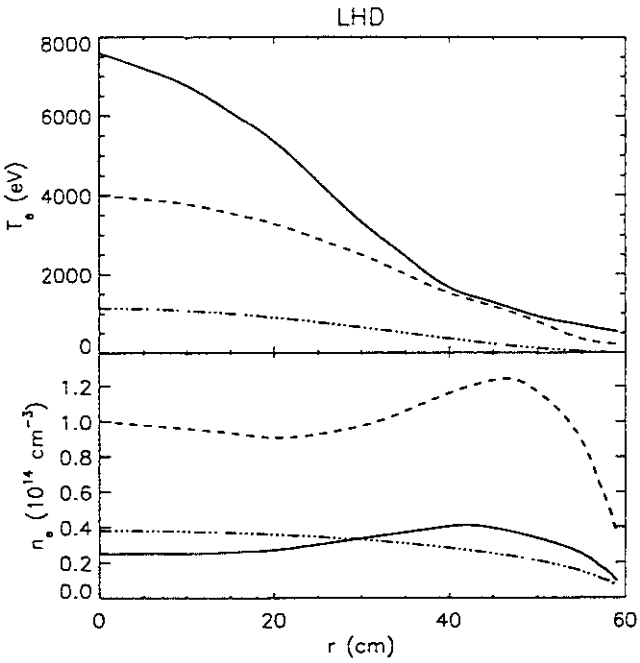

Fig.1

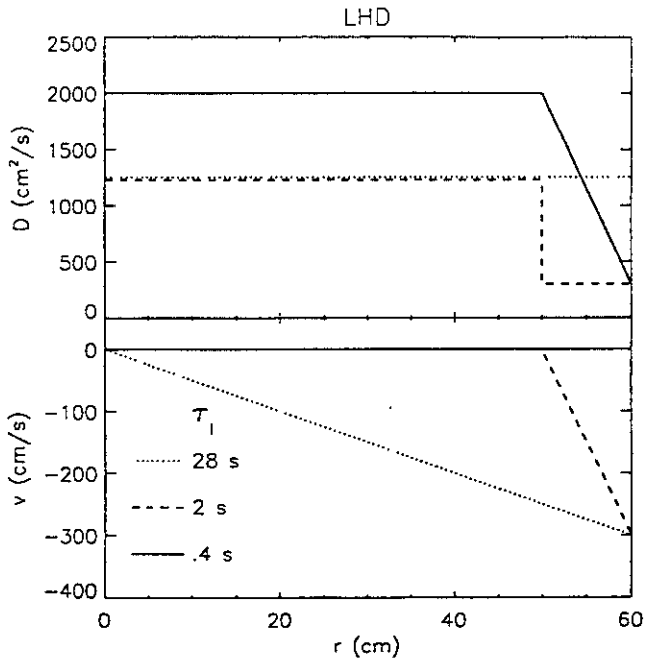

Fig.2

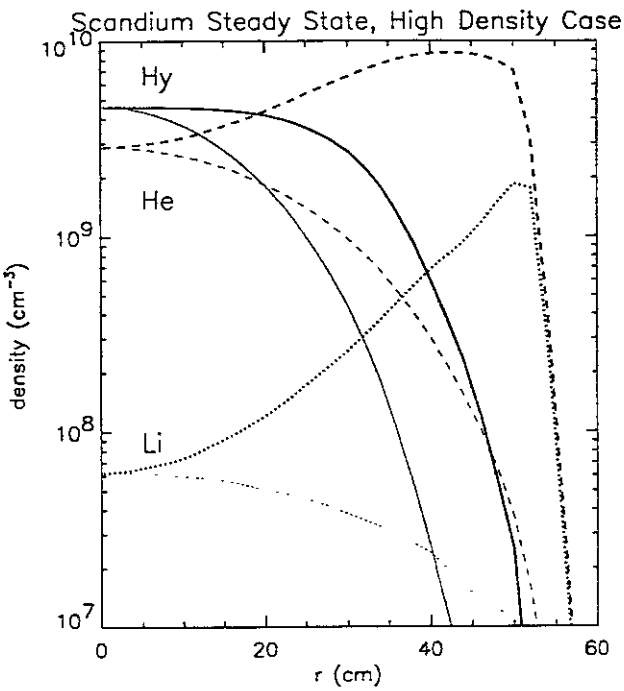

Fig.3

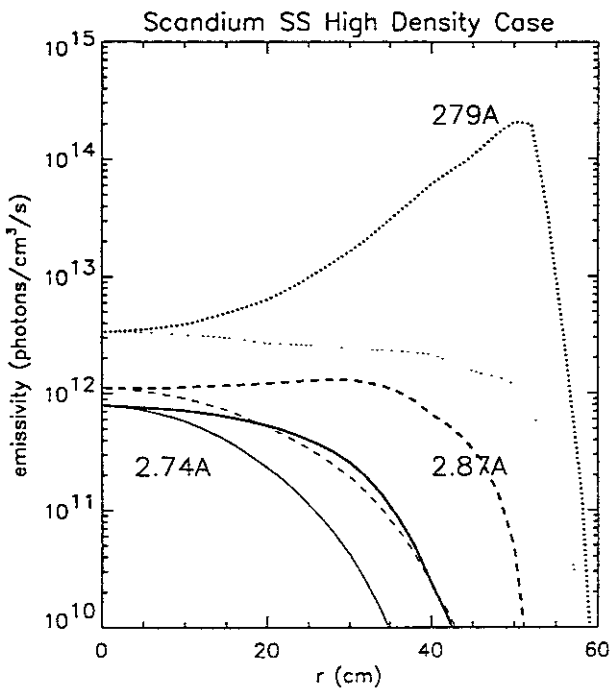

Fig.4

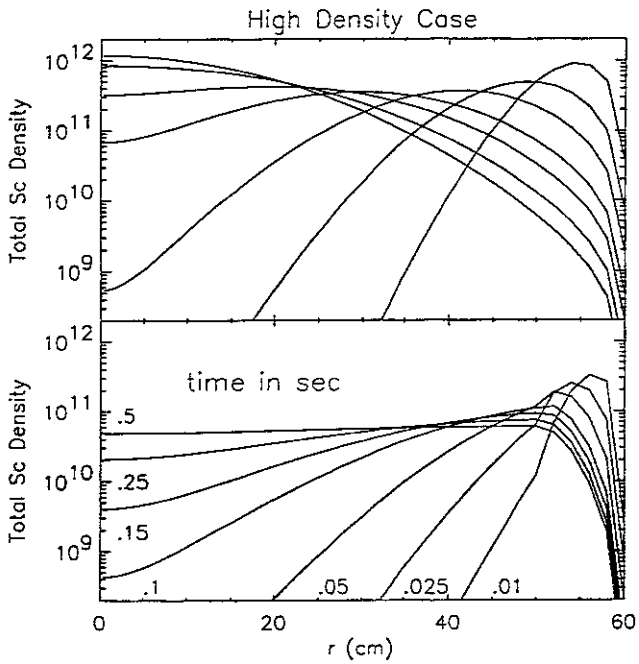

Fig.5

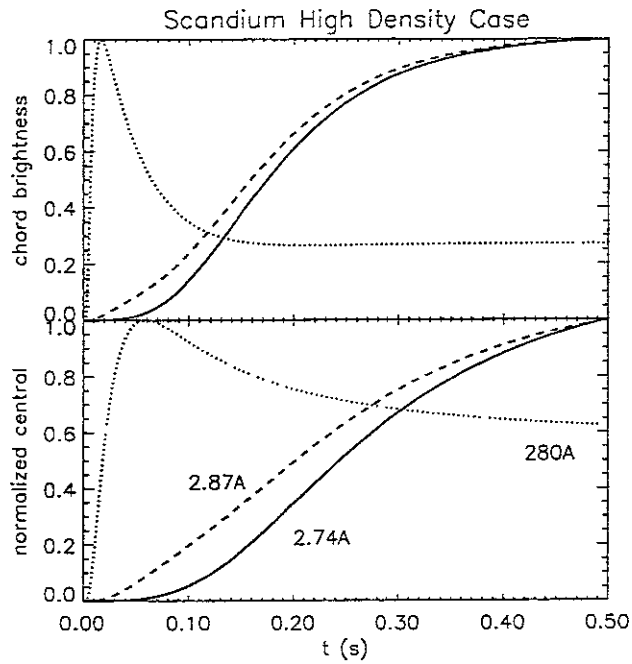

Fig.6

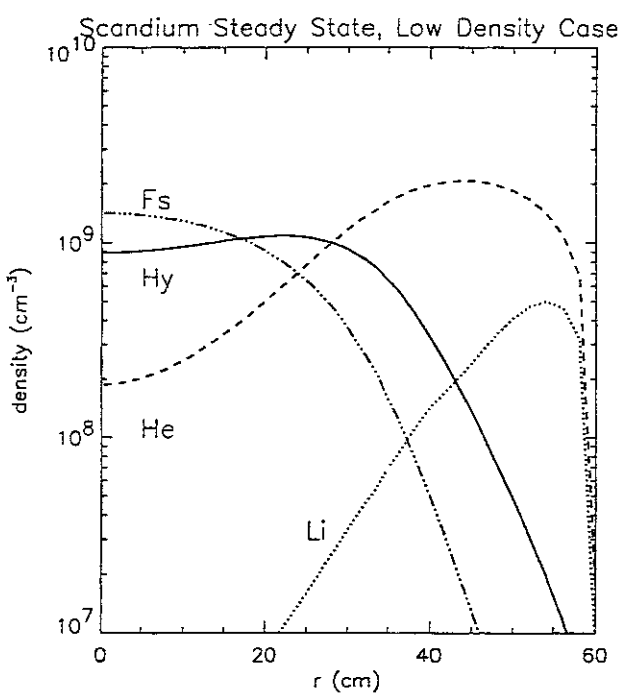

Fig.7

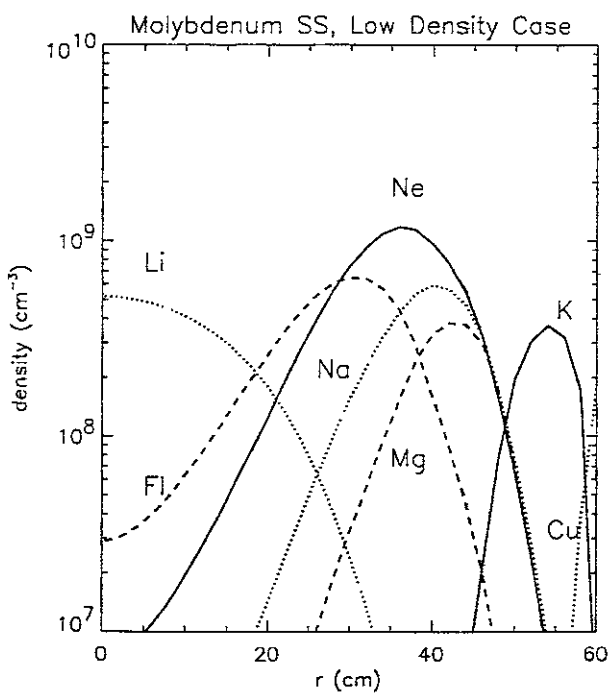

Fig.8

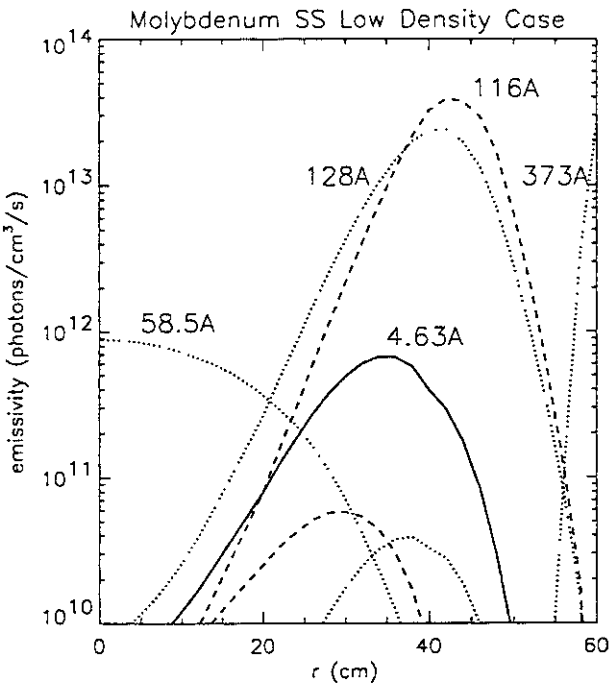

Fig.9

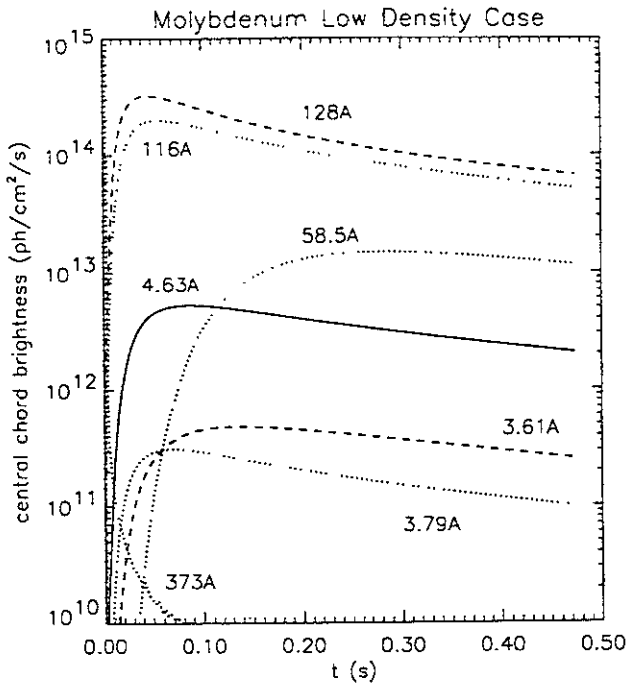

Fig.10

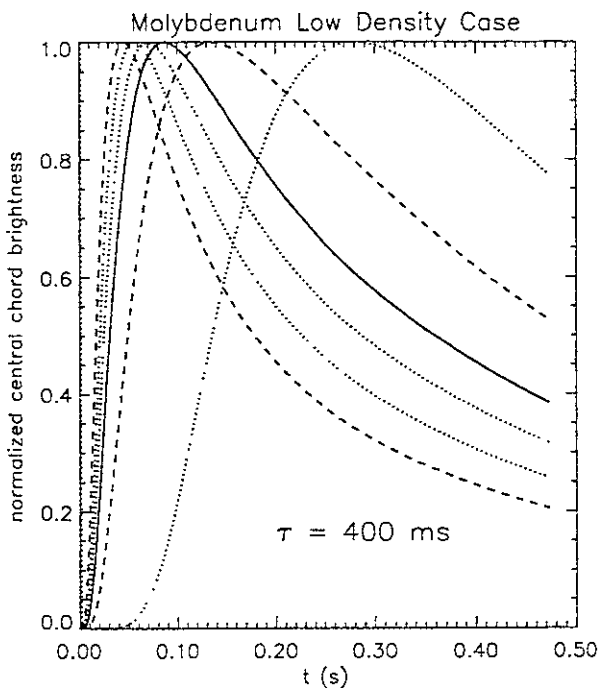

Fig.11

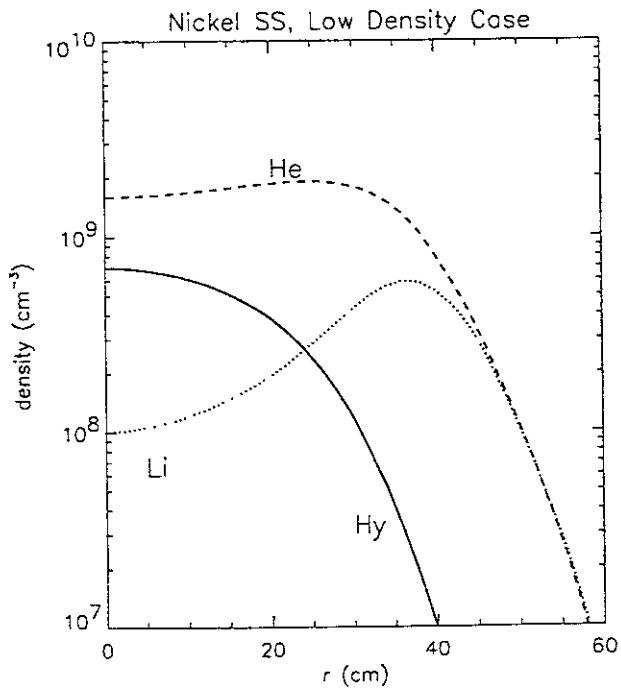

Fig.12

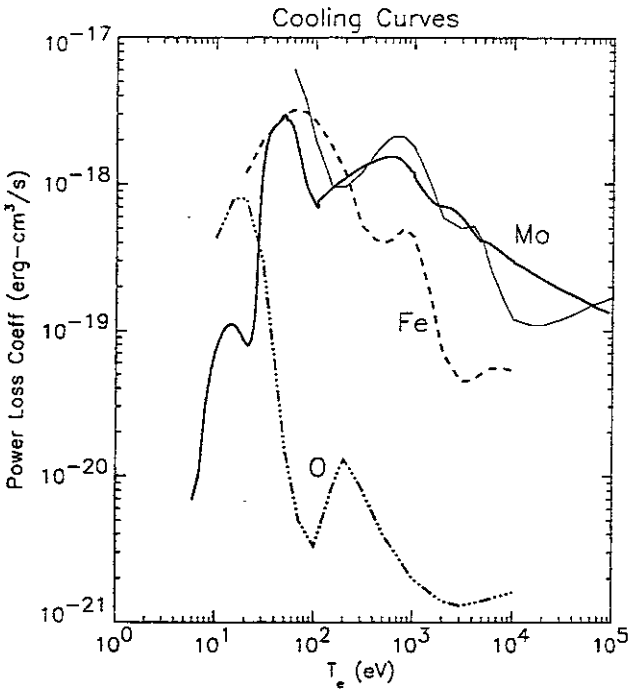

Fig.13

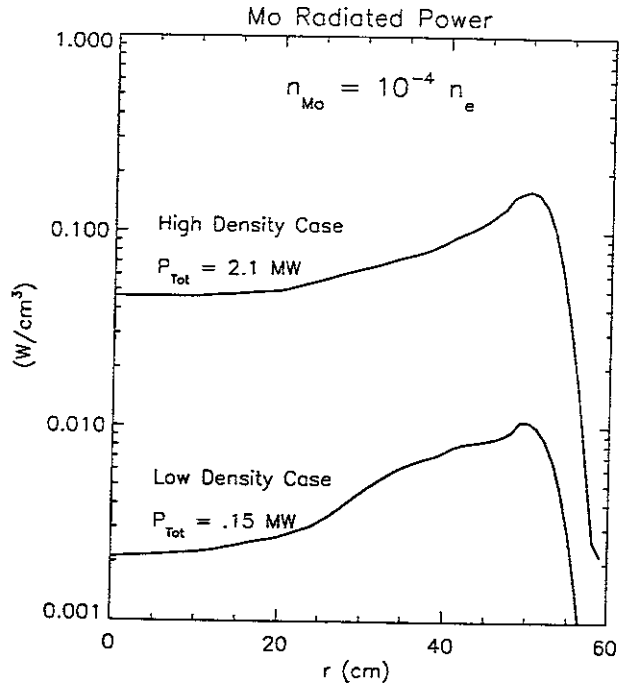

Fig.14

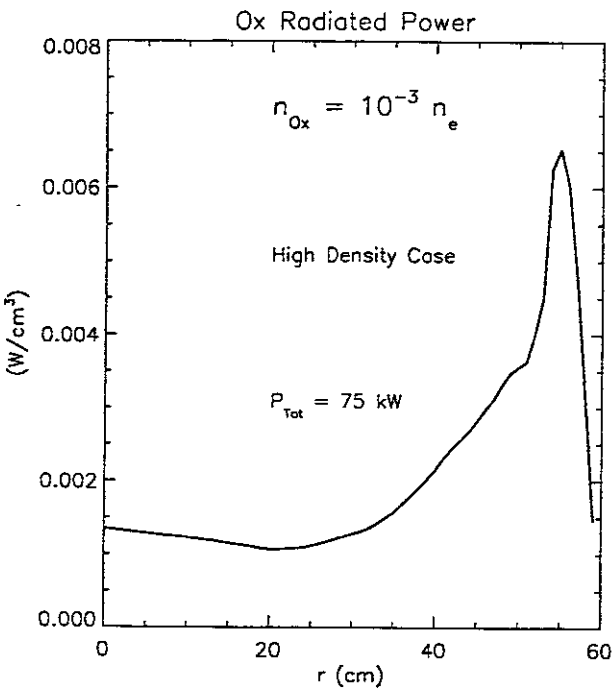

Fig.15

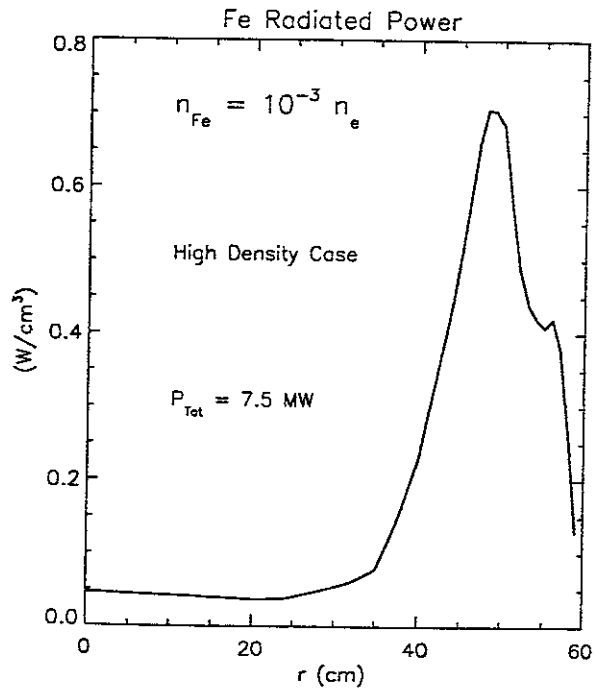

Fig.16

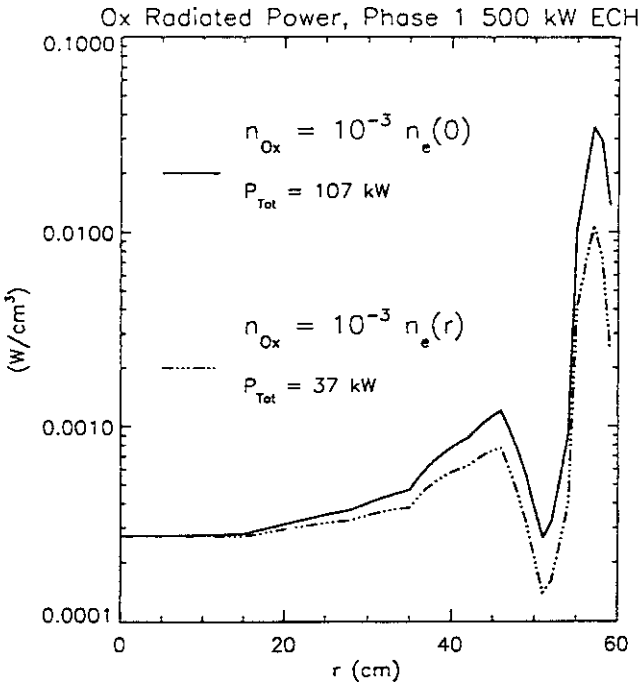

Fig.17

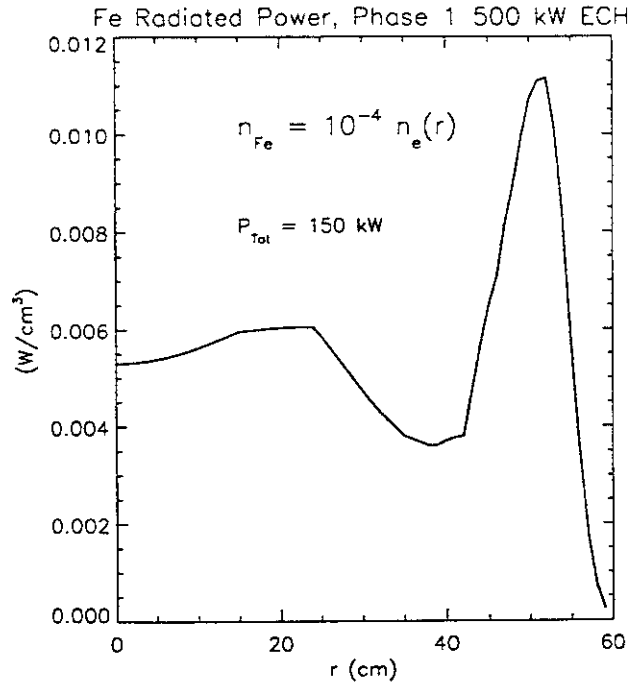

Fig.18

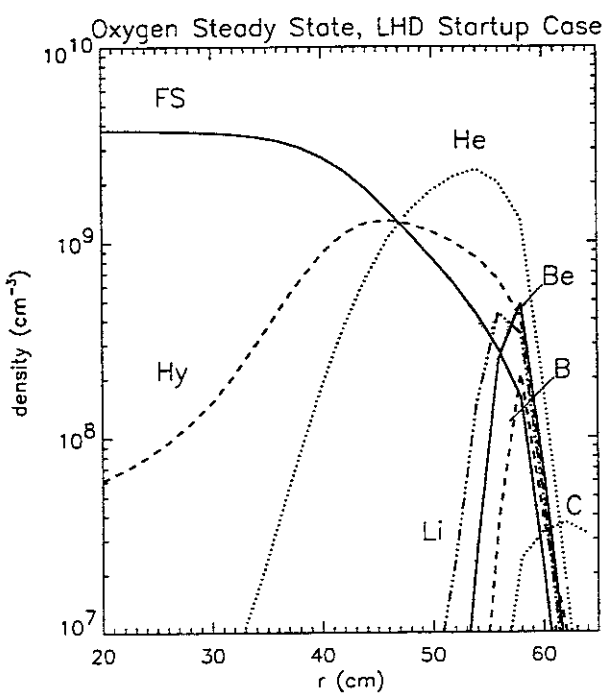

Fig.19

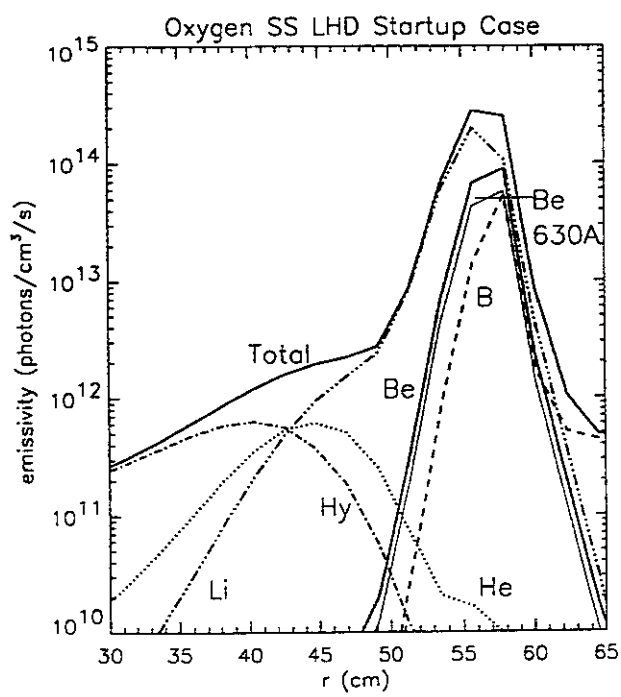

Fig.20

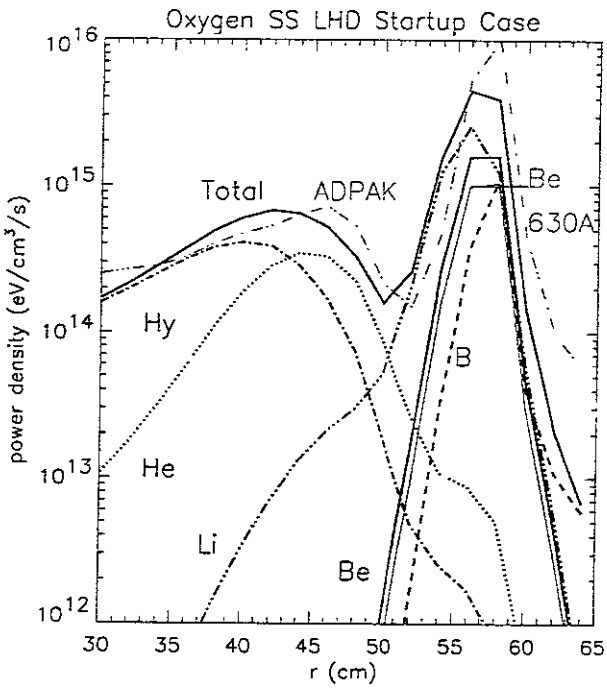

Fig.21

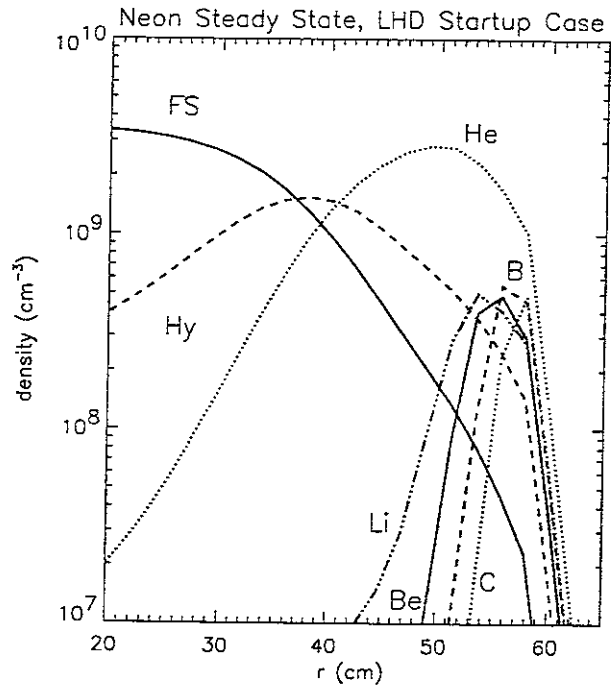

Fig.22

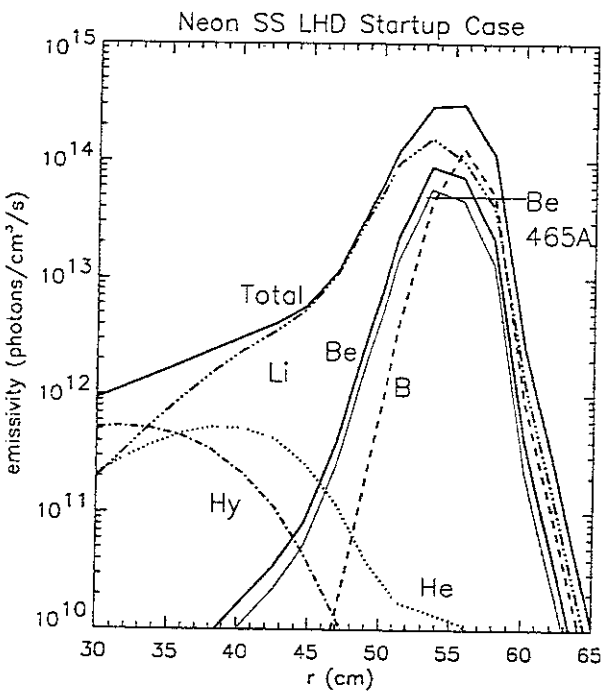

Fig.23

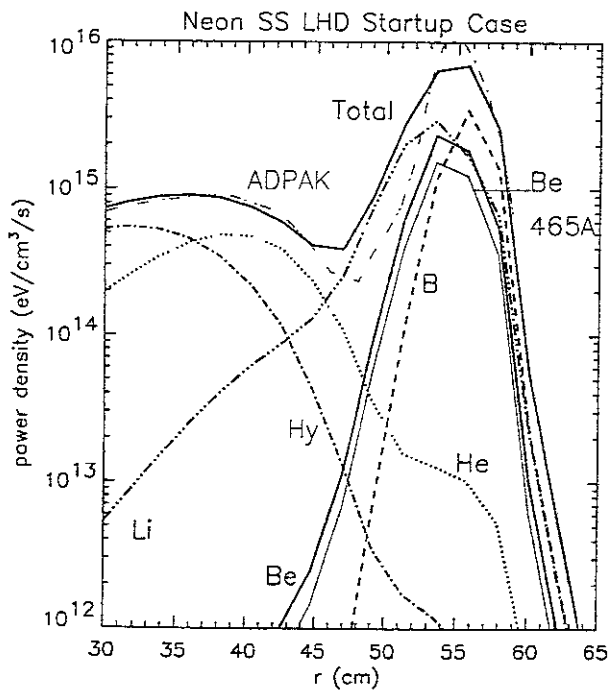

Fig.24

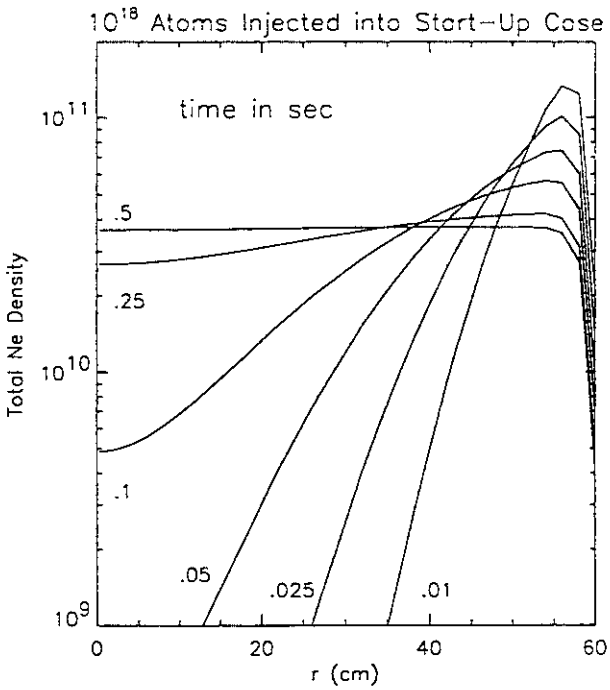

Fig.25

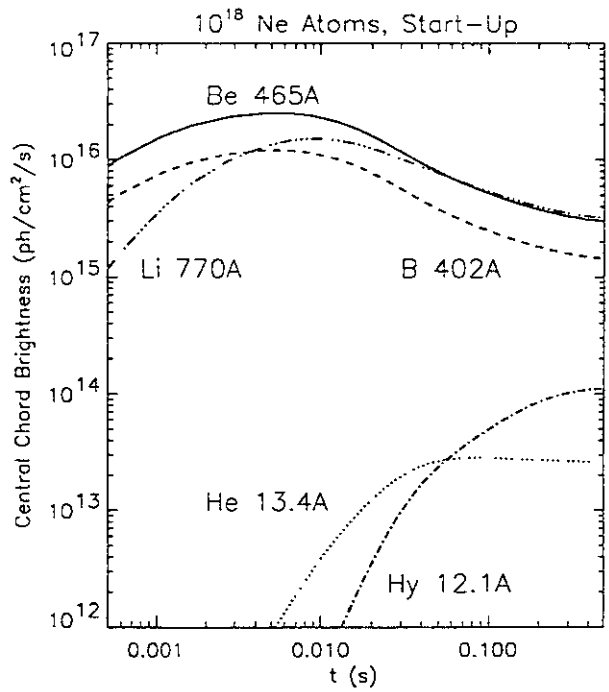

Fig.26

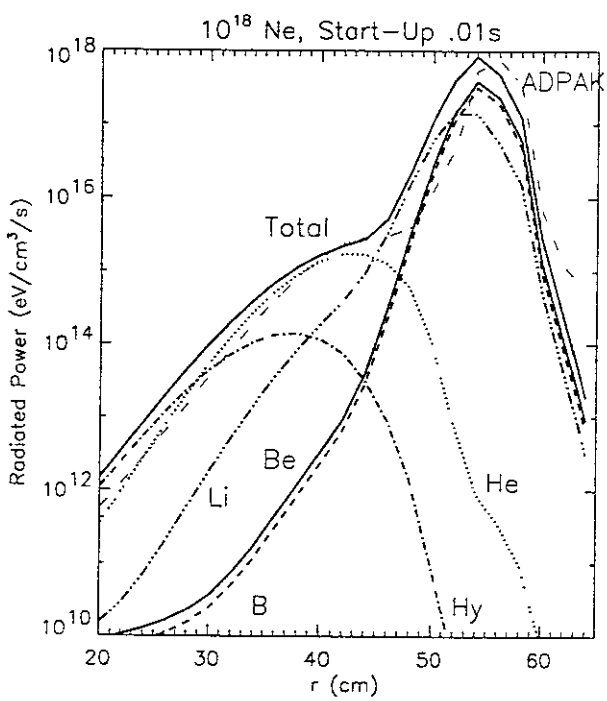

Fig.27

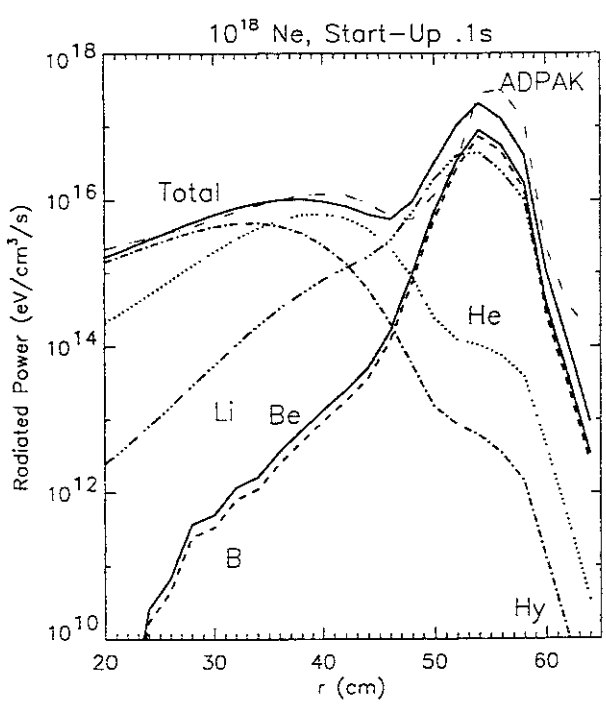

Fig.28

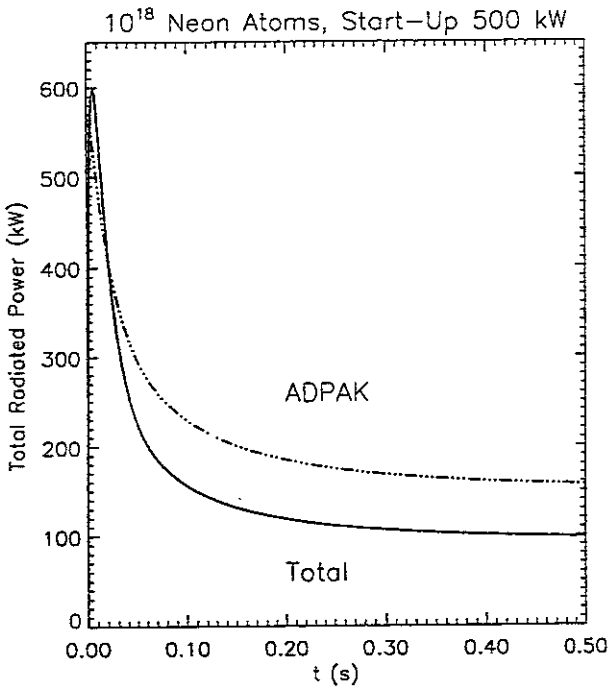
10^{18} Neon Atoms, Start–Up 500 kW
Total Radiated Power (kW)
600
500
400
300
200
100
0
ADPAK
Total
0.00
0.10
0.20
0.30
0.40
0.50
t (s)

Fig.29

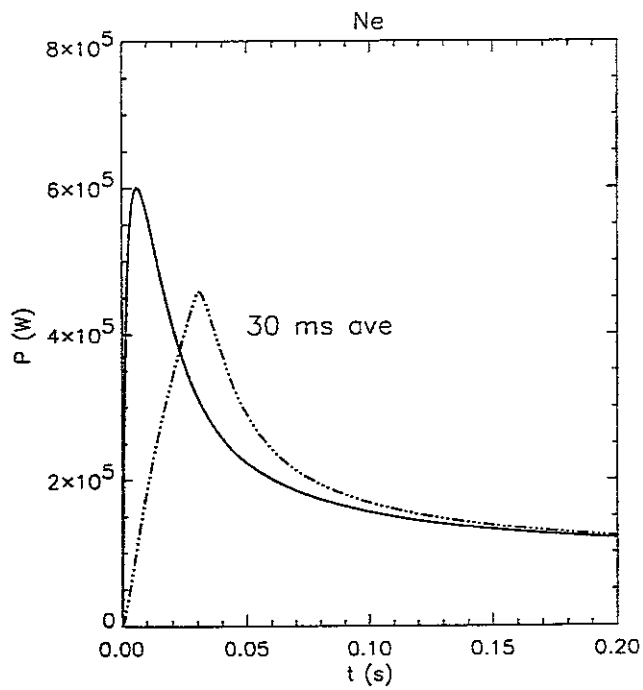
Ne
P (W)
8×10^5
6×10^5
4×10^5
2×10^5
0
30 ms ave
0.00
0.05
0.10
0.15
0.20
t (s)

Fig.30

Recent Issues of NIFS Series

NIFS-512 J Uramoto,
Clear Detection of Negative Pionlike Particles from H_2 Gas Discharge in Magnetic Field, Oct 1997

NIFS-513 T Shimozuma, M Sato, Y Takita, S. Ito, S Kubo, H. Idei, K Ohkubo, T Watari, T S Chu, K Felch, P Cahalan and C.M Loring, Jr,
The First Preliminary Experiments on an 84 GHz Gyrotron with a Single-Stage Depressed Collector; Oct 1997

NIFS-514 T Shimozuma, S. Morimoto, M. Sato, Y. Takita, S. Ito, S Kubo, H. Idei, K. Ohkubo and T Watari,
A Forced Gas-Cooled Single-Disk Window Using Silicon Nitride Composite for High Power CW Millimeter Waves; Oct. 1997

NIFS-515 K. Akaishi,
On the Solution of the Outgassing Equation for the Pump-down of an Unbaked Vacuum System; Oct 1997

NIFS-516 *Papers Presented at the 6th H-mode Workshop (Seeon, Germany)*; Oct 1997

NIFS-517 John L Johnson,
The Quest for Fusion Energy; Oct. 1997

NIFS-518 J Chen, N. Nakajima and M. Okamoto,
Shift-and-Inverse Lanczos Algorithm for Ideal MHD Stability Analysis; Nov 1997

NIFS-519 M. Yokoyama, N. Nakajima and M. Okamoto,
Nonlinear Incompressible Poloidal Viscosity in L=2 Heliotron and Quasi-Symmetric Stellarators; Nov. 1997

NIFS-520 S Kida and H. Miura,
Identificaiton and Analysis of Vortical Structures, Nov. 1997

NIFS-521 K. Ida, S. Nishimura, T. Minami, K. Tanaka, S. Okamura, M. Osakabe, H. Idei, S. Kubo, C. Takahashi and K Matsuoka,
High Ion Temperature Mode in CHS Heliotron/torsatron Plasmas; Nov. 1997

NIFS-522 M. Yokoyama, N. Nakajima and M. Okamoto,
Realization and Classification of Symmetric Stellarator Configurations through Plasma Boundary Modulations; Dec. 1997

NIFS-523 H. Kitauchi,
Topological Structure of Magnetic Flux Lines Generated by Thermal Convection in a Rotating Spherical Shell; Dec 1997

NIFS-524 T. Ohkawa,
Tunneling Electron Trap, Dec 1997

NIFS-525 K. Itoh, S.-I. Itoh, M. Yagi, A. Fukuyama,
Solitary Radial Electric Field Structure in Tokamak Plasmas, Dec 1997

NIFS-526 Andrey N. Lyakhov,
Alfven Instabilities in FRC Plasma; Dec. 1997

NIFS-527 J Uramoto,
Net Current Increment of negative Muonlike Particle Produced by the Electron and Positive Ion Bunch-method, Dec. 1997

NIFS-528 Andrey N. Lyakhov,
Comments on Electrostastic Drift Instabilities in Field Reversed Configuraiton; Dec. 1997

NIFS-529 J. Uramoto,
Pair Creation of Negative and Positive Pionlike (Muonlike) Particle by Interaction between an Electron Bunch and a Positive Ion Bunch; Dec. 1997

NIFS-530 J. Uramoto,
Measuring Method of Decay Time of Negative Muonlike Particle by Beam Collector Applied RF Bias

Voltage; Dec. 1997

NIFS-531 J. Uramoto,
Confirmation Method for Metal Plate Penetration of Low Energy Negative Pionlike or Muonlike Particle Beam under Positive Ions; Dec. 1997

NIFS-532 J. Uramoto,
Pair Creations of Negative and Positive Pionlike (Muonlike) Particle or K Mesonlike (Muonlike) Particle in H2 or D2 Gas Discharge in Magnetic Field; Dec. 1997

NIFS-533 S. Kawata, C. Boonmee, T. Teramoto, L. Drska, J. Limpouch, R. Liska, M. Sinor,
Computer-Assisted Particle-in-Cell Code Development; Dec. 1997

NIFS-534 Y. Matsukawa, T. Suda, S. Ohnuki and C. Namba,
Microstructure and Mechanical Property of Neutron Irradiated TiNi Shape Memory Alloy; Jan. 1998

NIFS-535 A. Fujisawa, H. Iguchi, H. Idei, S. Kubo, K. Matsuoka, S. Okamura, K. Tanaka, T. Minami, S. Ohdachi, S. Morita, H. Zushi, S. Lee, M. Osakabe, R. Akiyama, Y. Yoshimura, K. Toi, H. Sanuki, K. Itoh, A. Shimizu, S. Takagi, A. Ejiri, C. Takahashi, M. Kojima, S. Hidekuma, K. Ida, S. Nishimura, N. Inoue, R. Sakamoto, S.-I. Itoh, Y. Hamada, M. Fujiwara,
Discovery of Electric Pulsation in a Toroidal Helical Plasma; Jan. 1998

NIFS-536 Lj.R. Hadzievski, M.M. Skoric, M. Kono and T. Sato,
Simulation of Weak and Strong Langmuir Collapse Regimes; Jan. 1998

NIFS-537 H. Sugama, W. Horton,
Nonlinear Electromagnetic Gyrokinetic Equation for Plasmas with Large Mean Flows; Feb. 1998

NIFS-538 H. Iguchi, T.P. Crowley, A. Fujisawa, S. Lee, K. Tanaka, T. Minami, S. Nishimura, K Ida, R. Akiyama, Y. Hamada, H., Idei. M. Isobe, M. Kojima, S. Kubo, S. Morita, S. Ohdachi, S. Okamura, M. Osakabe, K. Matsuoka, C. Takahashi and K. Toi,
Space Potential Fluctuations during MHD Activities in the Compact Helical System (CHS); Feb. 1998

NIFS-539 Takashi Yabe and Yan Zhang,
Effect of Ambient Gas on Three-Dimensional Breakup in Coronet Formation Process; Feb. 1998

NIFS-540 H. Nakamura, K. Ikeda and S. Yamaguchi,
Transport Coefficients of InSb in a Strong Magnetic Field; Feb. 1998

NIFS-541 J. Uramoto,
Development of ν_μ Beam Detector and Large Area ν_μ Beam Source by H_2 Gas Discharge (I); Mar. 1998

NIFS-542 J. Uramoto,
Development of bar{ν}$_\mu$ Beam Detector and Large Area bar{ν}$_\mu$ Beam Source by H_2 Gas Discharge (II); Mar. 1998

NIFS-543 J. Uramoto,
Some Problems inside a Mass Analyzer for Pions Extracted from a H_2 Gas Discharge; Mar. 1998

NIFS-544 J. Uramoto,
Simplified ν_μ, bar{ν}$_\mu$ Beam Detector and ν_μ, bar{ν}$_\mu$ Beam Source by Interaction between an Electron Bunch and a Positive Ion Bunch; Mar. 1998

NIFS-545 J. Uramoto,
Various Neutrino Beams Generated by D_2 Gas Discharge; Mar 1998

NIFS-546 R. Kanno, N. Nakajima, T. Hayashi and M. Okamoto,
Computational Study of Three Dimensional Equilibria with the Bootstrap Current; Mar. 1998

NIFS-547 R. Kanno, N. Nakajima and M. Okamoto,
Electron Heat Transport in a Self-Similar Structure of Magnetic Islands; Apr. 1998

NIFS-548 J.E. Rice,
Simulated Impurity Transport in LHD from MIST; May 1998